Journal of Environmental Chemical Engineering 14 (2026) 122865

Contents lists available at ScienceDirect

Journal of Environmental Chemical Engineering

journal homepage: www.elsevier.com/locate/jece

A V-shaped CNT-decorated $LiNi_{0.8}Co_{0.15}Al_{0.05}O_2$ photothermal fabric for high-efficiency solar steam generation and desalination

Huibin Guan [a], Naila Arshad [b], Bushra Shakoor [c], Najah Alwadie [d], Xiaochao Fan [a,*], Ruijing Shi [a], Van-Duong Dao [e,*], Nang Xuan Ho [e], Jian Zhang [f,*], Muhammad Sultan Irshad [b], Calvyn T. Howells [g], Phuong Anh Lam [h], Iftikhar Ahmed [g,*]

[a] College of Energy Engineering, Xinjiang Institute of Engineering, Urumqi, 830023, China
[b] Ministry of Education Key Laboratory of Green Preparation and Application for Functional Materials, School of New Energy and Electrical Engineering, Hubei University, Wuhan 430062, China
[c] Department of Chemistry, University of Wah, Wah Cantt 47040, Pakistan
[d] Department of Physics, College of Science, Princess Nourah bint Abdulrahman University, P.O. Box 84428, Riyadh 11671, Saudi Arabia
[e] Faculty of Biotechnology, Chemistry, and Environmental Engineering, Phenikaa School of Engineering, Phenikaa University, Hanoi 12116, Viet Nam
[f] Institute of Materials Science and Devices, School of Materials Science and Engineering, Suzhou University of Science and Technology, Suzhou 215009, China
[g] Environmental and Public Health Department College of Health Sciences Abu Dhabi University, P.O. Box, 59911, Abu Dhabi, United Arab Emirates
[h] Department of Chemistry, Case Western Reserve University, 10900 Euclid Avenue, Cleveland, OH 44106, USA

ARTICLE INFO

Editor: Wen-Yueh Yu

Keywords:
Solar steam generation
NCAL@CNTs
V-shaped evaporator
Desalination
Thermal management

ABSTRACT

Addressing global water scarcity requires sustainable and efficient water purification technologies. Solar-driven interfacial evaporation (SDIE) has emerged as a promising and sustainable technology that utilizes abundant solar energy. However, its efficiency is frequently constrained by inadequate photothermal materials, heat loss, salt accumulation, and an inability to remove soluble contaminants. Herein, we develop a novel photothermal V-shaped photonic harvester by incorporating $LiNi_{0.8}Co_{0.15}Al_{0.05}O_2$ (NCAL) decorated with multi-walled carbon nanotubes (NCAL@CNTs) nanocomposites onto a hydrophilic nonwoven fabric. The NCAL nanoparticles ensure broadband solar absorption in the near-infrared region, while the CNT network offers remarkable thermal conductivity, accelerates vapor diffusion, and enhances mechanical integrity. Consequently, this synergistic integration yields an exceptionally efficient solar evaporation system. Under 1 sun illumination (1 kW m^{-2}), the optimized NCAL@CNTs fabric demonstrates an outstanding evaporation rate of 2.30 kg m^{-2} h^{-1} with a corresponding solar-thermal efficiency of 91.4%. Additionally, the fabric shows excellent multifunctional purification capabilities and effectively desalinates simulated seawater, achieving ion-rejection rates exceeding 99.9%. This work establishes scalable and multifunctional solar evaporation for practical freshwater production.

1. Introduction

The global challenge of water scarcity necessitates the development of sustainable and efficient technologies for freshwater production [1]. Using the abundant energy of sunlight to produce clean water, solar-driven interfacial evaporation (SDIE) has become a viable and environmentally friendly option [2,3]. SDIE systems significantly increase energy conversion efficiency by localizing heat at the air-water interface through a floating photothermal evaporator, in contrast to conventional bulk heating techniques that suffer from substantial heat loss [4,5]. This technology is developing from basic material investigation to the development of integrated, multifunctional systems that can meet more extensive water and energy requirements [6].

The characteristics of an SDIE system's photothermal material have a significant impact on its performance. Because of their superior broadband light absorption, high thermal conductivity, and porous structure that promotes water transport and vapor escape, carbon nanotubes (CNTs) have become a leading material in the field [7,8]. As an illustration of the potential of carbon-based materials in integrated systems, multi-functional CNT papers have shown remarkable evaporation rates

* Corresponding authors.
E-mail addresses: fxc1979@xju.edu.cn (X. Fan), duong.daovan@phenikaa-uni.edu.vn (V.-D. Dao), jianzhang@xju.edu.cn (J. Zhang), Dr.Iftikhar.Ahmed@live.fr (I. Ahmed).

https://doi.org/10.1016/j.jece.2026.122865
Received 5 February 2026; Received in revised form 7 April 2026; Accepted 25 April 2026
Available online 26 April 2026

of 1.28 kg m^{-2} h^{-1} under 1 sun irradiation, combined with capabilities for thermoelectric generating and energy storage [9,10]. However, the pursuit of even greater material diversity, reduced cost, and improved performance is still ongoing. Combining CNTs with additional photothermal agents to create composites is an appealing way to enhance performance. This approach has proven effective, as demonstrated by studies such as the incorporation of copper sulfide (CuS) with carbon nanotubes (CNTs) to create a hierarchical structure that achieved a high evaporation rate of 1.50 kg m^{-2} h^{-1} under 1 sun illumination by improving light absorption and thermal management [11,12].

Motivated by these synergistic effects, we present the usage of a layered mixed metal oxide as a new and powerful companion for CNTs: $LiNi_{0.8}Co_{0.15}Al_{0.05}O_2$ (NCAL). The unique composition of NCAL, which was previously researched for energy storage, makes it a great option for photothermal conversion. It has a matrix rich in nickel for strong solar absorption, complemented by cobalt and aluminum [13,14]. Its combination with CNTs is intended to produce a composite that combines the advantages of both materials, possibly resulting in improved heat localization and light harvesting. Beyond material composition, rational thermal management is paramount for maximizing efficiency [15]. Conduction can cause a large amount of solar energy to be lost to the underlying bulk water. Although polyurethane (PU) foam substrates are frequently used for thermal insulation [16,17], their geometry can be designed to further reduce losses. As a "heat trap," the creation of a V-shaped cavity in the foam efficiently stores thermal energy just below the evaporative surface [18,19].

Herein, we present a high-performance and multifunctional solar evaporator, whose integrated design and working principle are schematically illustrated in Fig. 1. The system consists of a structurally designed PU foam with a V-shaped cavity on top of a photothermal layer of unique NCAL and carbon nanotube (NCAL@CNT) composite that is deposited onto a flexible nonwoven (NW) fabric using a straightforward slurry-coating approach. This assembly floats on a water source. When exposed to solar radiation, the composite's wide light absorption and efficient photothermal conversion quickly produce heat, which is confined inside the V-shaped cavity to promote effective steam generation at the interface. At the same time, a constant capillary-fed water supply is made possible by the hydrophilic fabric and porous foam. These functional groups interact with metal ions in solutions (such as Pb^{2+}, Co^{2+}, Na^{+}, and Ca^{2+}) to help purify water through ion-exchange and surface complexation mechanisms. Importantly, as shown, this design naturally reduces salt accumulation and ensures operational stability by encouraging the downward diffusion of ions (such as Na^{+} and Cl^{-}) away from the hot evaporation front and back into the bulk water. This study provides a comprehensive evaluation of the system's performance, emphasizing its high rate of evaporation, long-term stability because of its durable composite structure and anti-salt accumulation design, and exceptional efficacy in removing heavy metal and common metal ions, indicating a significant advancement toward useful and versatile solar water purification systems.

2. Methodology

2.1. Materials

Lithium Nickel Cobalt Aluminum Oxide ($LiNi_{0.8}Co_{0.15}Al_{0.05}O_2$, NCAL) powder (battery grade, $\geq$ 99.8% purity) was procured from Xiamen Tob New Energy Technology Co., Ltd. (China). Multi-walled carbon nanotubes (MWCNTs, > 95% purity, outer diameter: 10–20 nm, length: 10–30 μm) were supplied by Beijing DK Nano Technology Co., Ltd. (China). The non-woven fabric (100% polyester, areal density: 80 g m^{-2}, thickness: ~0.3 mm) was obtained from a local supplier. Commercial PU foam (density: 22 kg m^{-3}, porosity: > 95%) was used as the insulating substrate. Polyvinyl alcohol ($(C_2H_4O)_x$, PVA) was used as a binder and was purchased from Sigma-Aldrich. All chemicals were used as received without further purification.

2.2. Fabrication of NCAL@CNTs-NW fabric evaporator

A straightforward slurry coating method was used to develop the photothermal evaporator. First, a 1:1 mass ratio mixture of MWCNTs and NCAL powder was dispersed in an aqueous solution containing 1.5 wt% PVA to form a homogenous and stable slurry. For every 10 ml of PVA solution, the combined mass of the active ingredients (NCAL and CNTs) was 200 mg. After an hour of vigorous magnetic stirring to create a preliminary dispersion, the mixture was exposed to 30 min of probe sonication in an ice bath to break up agglomerates and produce a homogenous, coatable slurry. Using a soft-bristle brush, this slurry was then manually applied to a pre-cleaned rectangular piece of non-woven fabric (diameter: 6 cm×4 cm), providing a uniform and adhesive layer throughout the substrate surface. In order to remove water and solidify the PVA binder, the coated fabric was placed in a vacuum oven and dried at 70 °C for 12 h. This produced a strong and integrated NCAL@CNTs composite layer that was firmly bound to the fabric and was thereafter referred to as NCAL@CNT-NW fabric. For the final assembly, a V-shaped cavity was carved into a rectangular block of PU foam to act as a thermal insulator and water transport pathway.

2.3. Material characterization

A Field Emission Scanning Electron Microscope (FESEM, JSM-7100F, JEOL, Japan), when combined with an Energy Dispersive X-ray Spectrometer (EDX), was used to examine the surface morphology and elemental composition of the generated NCAL@CNTs-NW fabric. Using a THERMO FISHER SCIENTIFIC Escalab 250Xi equipment with a monochromatic Al Kα X-ray source, X-ray photoelectron spectroscopy (XPS) was employed to examine the chemical states and elemental composition of the NCAL@CNTs composite. The functional groups on

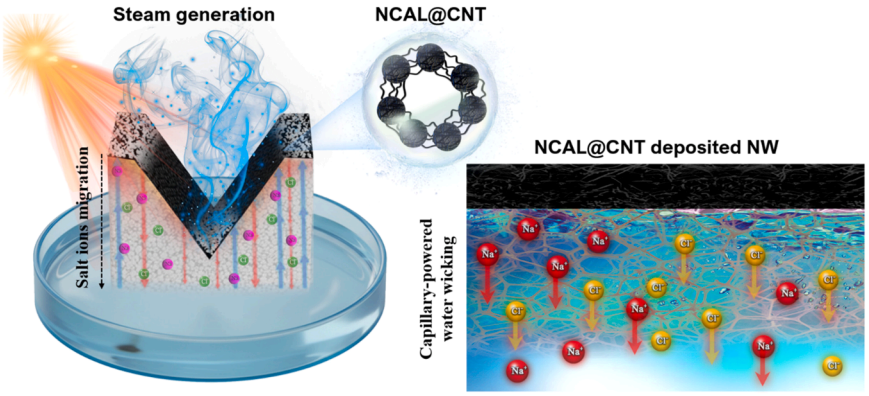

Fig. 1. Schematic illustration of the NCAL@CNT-NW fabric solar evaporator and its working mechanism.

the material surfaces were identified using Fourier-Transform Infrared (FTIR) spectroscopy (Nicolet iS50, Thermo Scientific) in the 500–4000 cm^{-1} range. A Shimadzu UV-3600i Plus UV-Vis-NIR spectrophotometer with an integrating sphere was used to assess the optical absorption characteristics throughout the solar spectrum (250–2500 nm). A thermal constants analyzer (Hot Disk TPS 2500S) based on the transient plane source method was used to measure the thermal conductivity of the pristine PU foam and the integrated evaporator assembly at room temperature.

2.4. Solar evaporation and water purification performance evaluation

Employing a Class AAA solar simulator (PerfectLight, PLS-SXE300D) calibrated to generate an AM 1.5 G spectral irradiation at 1 kW m^{-2} (1 sun), solar-driven evaporation tests were carried out under ambient laboratory conditions (25 ± 2 °C, 50 ± 5% relative humidity). The V-shaped PU foam and the assembled NCAL@CNT-NW fabric evaporator floated on the surface of the aqueous solution in a tailored glass vessel. Deionized (DI) water, 3.5 wt% common metal ions (Na^+, K^+, Mg^{2+}, Ca^{2+}), and artificial wastewater with heavy metal ions (e.g., 100 ppm Cu^{2+}, 100 ppm Co^{2+}, 100 ppm Fe^{3+}, and 100 ppm Pb^{2+}) were among the solutions examined. A high-precision analytical balance (Mettler Toledo, ME204/02, 0.1 mg resolution) was used to record the mass change of the complete system in real-time at 10-second intervals. To create a stable baseline and guarantee thermal equilibrium, each test was preceded by a 30-minute stabilization period in the dark. The mass loss data collected during 60 min under steady-state illumination were used to calculate the evaporation rate.

An infrared thermal camera (FLIR, E60) was used for measuring the evaporator's surface temperature distribution and thermal localization. Throughout the experiment, the thermal profiles of the bulk water, the V-shaped cavity, and the evaporation surface were recorded. A laboratory-scale condensation setup was utilized to collect the condensed vapor during an 8-hour irradiation period in order to assess the purifying efficacy of the system. An Inductively Coupled Plasma Optical Emission Spectrometer (ICP-OES, PerkinElmer, Avio 500) was applied to measure the concentrations of primary ions (Na^+, K^+, Mg^{2+}, Ca^{2+}) and heavy metal ions (Cu^{2+}, Co^{2+}, Fe^{2+}, Pb^{2+}) in the initial feed solution and the collected condensate to calculate the ion rejection efficiency. The versatility of the NCAL@CNT-NW evaporator was evaluated in various water sources by monitoring the evaporation rate and structural integrity of the evaporator.

3. Results and discussion

The NCAL@CNT-NW fabric evaporator's excellent construction and thorough characterization confirm the photothermal composite's successful integration with the tailored V-shaped insulation. Results show that this design produces outstanding solar evaporation performance, characterized by high rates, long-term stability, and multifunctional purification capabilities. The X-ray diffraction (XRD) spectroscopy, X-ray photoelectron spectroscopy (XPS), and Fourier-transform infrared (FTIR) spectroscopy investigations, which are essential for elucidating the crystalline structure, chemical composition, elemental oxidation states, and surface functional groups of the developed NCAL@CNT composite, are shown in Fig. 2. These properties are closely related to the material's ability to adsorb metal ions and its photothermal conversion efficiency. XRD analysis was carried out to determine the crystalline phases and verify the NCAL@CNT composite's structural composition, as shown in Fig. 2a. The (003) plane of the NCAL phase is represented by a significant peak at about 18.6°, while the peak at ~26.1° is assigned to the (002) plane of graphitic CNTs, indicating that the carbon nanotubes were successfully incorporated. The existence of crystalline metal oxide/spinel phases is indicated by additional peaks in the ~36–68° range (including 101, 006, 104, 015, 107, 018, and 110 planes). This suggests that the NCAL is well integrated with CNTs to produce a stable hybrid composite. Fig. 2b shows the high-resolution XPS spectra of Ni 2p. The spectrum exhibits two primary spin-orbit

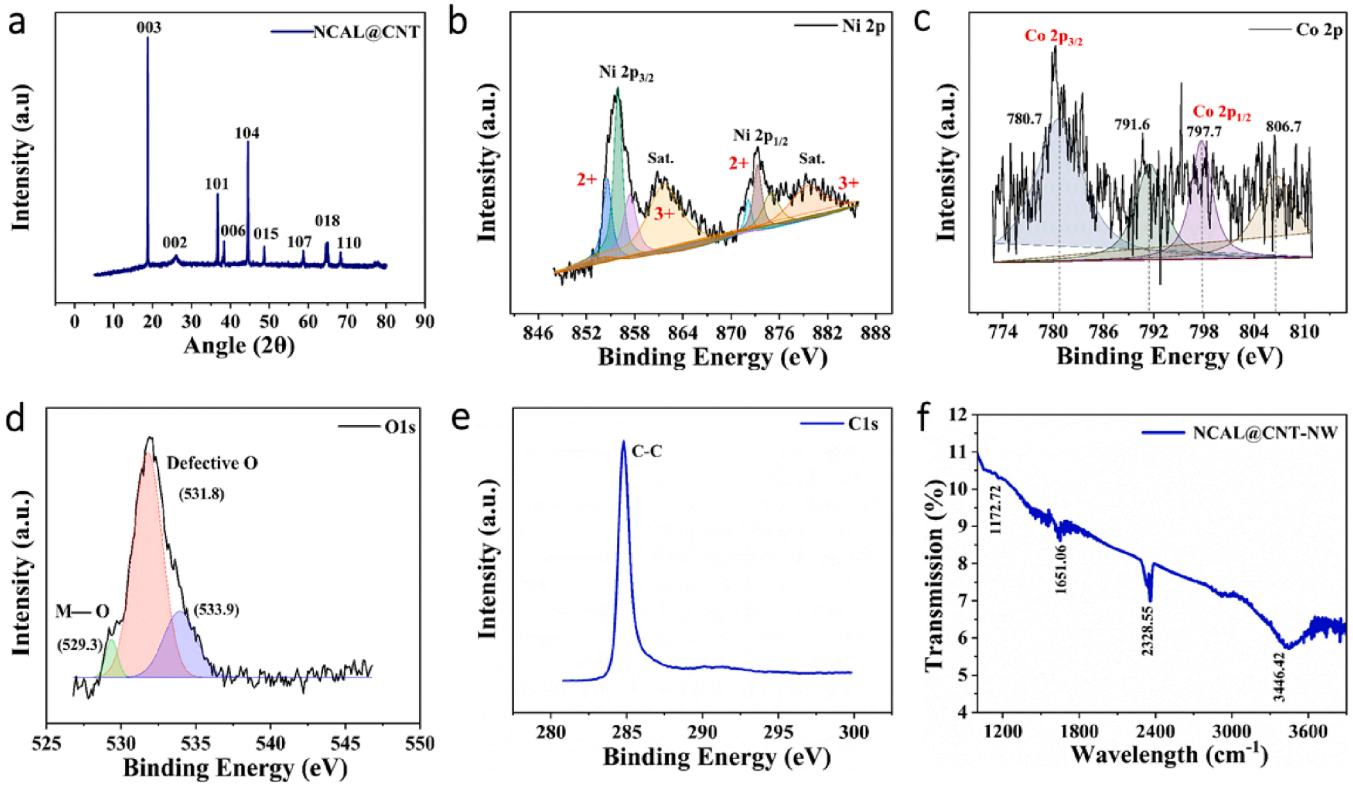

Fig. 2. Chemical state and surface functional group analysis of the NCAL@CNT-NW fabric. (a) XRD pattern of NCAL@CNT. High-resolution XPS spectrum of (b) Ni 2p, (c) Co 2p, (d) O 1 s, (e) C 1 s. (f) FTIR spectrum of the NCAL-CNT@NW fabric, showing bands corresponding to O-H, C═O, and C-O functional groups.

doubles. For Ni^{2+} in a Ni-O lattice configuration, the peaks at binding energies of around 855.9 eV and 873.2 eV are attributed to Ni $2p_{3/2}$ and Ni $2p_{1/2}$, respectively [20,21]. The co-existence of Ni^{3+} species is confirmed by the presence of prominent satellite features around 861.7 eV and 879.6 eV, as well as the peak component about 857.4 eV, suggesting a mixed Ni^{2+}/Ni^{3+} oxidation state typical of the layered NCAL structure [22]. This mixed valence state is beneficial for charge transfer processes, which can improve light absorption. The Co 2p spectrum, which is deconvoluted into two primary spin-orbit doublets, is displayed in Fig. 2c. The existence of cobalt in oxidized states is confirmed by the high-resolution XPS spectra of Co 2p, which displays two major spin–orbit peaks at 780.7 eV (Co $2p_{3/2}$) and 797.7 eV (Co $2p_{1/2}$). The existence of Co^{2+} species is indicated by the typical shake-up satellite peaks at ~791.6 eV and the wide feature at ~806.7 eV. The slight asymmetry of the main peaks suggests the coexistence of $Co^{2+}$and Co^{3+}, reflecting a mixed-valence state. The NCAL material's nominal composition is consistent with the simultaneous occurrence of both cobalt oxidation states, which also enhances the material's electrical conductivity. The O 1 s spectrum (Fig. 2d) is fitted with three components. The dominant peak at 529.3 eV is ascribed to lattice oxygen (M–O) in the metal oxide framework. The greater binding energy component at 533.9 eV is attributed to water or surface-adsorbed hydroxyl groups (-OH), while the peak at 531.8 eV is attributed to defective oxygen or oxygen vacancies. The sp^2-hybridized carbon (C-C/C═C) of the graphitic CNTs is represented by a significant peak at 284.8 eV in the composite's C 1 s spectra (Fig. 2e) [23]. The NCAL-CNT@NW composite's surface chemistry is further revealed by its FTIR spectrum (Fig. 2f). O-H stretching vibrations from adsorbed water and surface hydroxyl groups are characterized by the wide and strong band centered at 3446 cm^{-1}. C═O stretching vibrations from carboxyl groups are responsible for the band at 1651 cm^{-1}, while C-O stretching is indicated by the characteristic near 1173 cm^{-1} [24]. These functional groups, which originate from both the NCAL surface and the CNTs, improve the evaporator's hydrophilicity for effective water wicking and offer coordination sites for thermal localization.

Moreover, the NCAL@CNT composite's microstructural shape, which governs light absorption, heat management, and water transport within the solar evaporator, is revealed by the scanning electron microscope (SEM) investigation shown in Fig. 3. The system's excellent performance is based on the composite powder's porous architecture and its effective integration with the non-woven fabric substrate. The SEM images of the pure NCAL@CNT powder at various magnifications are shown in Fig. 3a–c. The powder shows a distribution of spherical ball-like structures (attributed to NCAL) scattered with thin, tube-like features (attributed to CNTs) at lower magnification (Fig. 3a). Higher magnification (Fig. 3b) reveals a network of CNTs decorating and connecting the spherical NCAL particles. A closer look (Fig. 3c) makes it evident that the CNTs are evenly distributed on the NCAL spheres' surface, creating a conformal coating. The structure is ideal for solar-driven interfacial evaporation because of the composite's rough and porous texture, which further improves light trapping through many scattering events [25]. The successful coating of this composite onto the fabric substrate is confirmed in Fig. 3d-f. The individual threads of the non-woven fabric, uniformly wrapped and coated with the NCAL@CNT composite, are clearly visible in the SEM images at various scales. While the coating layer appears irregular and particulate (Fig. 3e, f), it forms a continuous, adherent film on the fibrous network. A three-dimensional (3D) porous photothermal layer is generated using this microstructure. The irregularities and gaps within the coating, combined with the inherent porosity of the non-woven fabric, establish interconnected microchannels. These channels are vital for maintaining a high evaporation rate because they enable quick capillary-driven water wicking to the evaporation surface and provide unobstructed escape routes for produced vapor [26,27].

Furthermore, Fig. 4 analyzes the critical significance of structural engineering, specifically the implementation of a V-shaped cavity, in optimizing the thermal management of the solar evaporator. To enhance solar-thermal conversion efficiency and reduce energy losses, effective photon and heat confinement is crucial, surpassing the performance constraints imposed solely by material properties. The fundamental idea is explained by a direct comparison between the V-shaped design and a flat evaporator (Fig. 4a-b). The specular reflection of incident sunlight away from the surface results in a significant optical loss in the planar design. On the other hand, the V-shaped cavities' inclined walls serve as a light trap. To minimize reflecting losses, incident rays experience several internal reflections inside the cavity, which significantly increase the optical path length and increase the probability of absorption by the NCAL@CNT coating [28]. The schematic and associated infrared (IR) thermographic images (Fig. 4c-d) demonstrate how this higher optical absorption directly correlates to improved thermal localization. This illustrates how the structure effectively prevents the produced thermal energy from dissipating laterally or into bulk water by accurately restricting it at the air-water contact where evaporation takes place. Moreover, the optical absorption properties of the NCAL@CNT composite (Figure S1) demonstrate that the composite exhibits broadband absorption with a particularly strong response in the near-infrared region, consistent with the high photothermal conversion efficiency observed. A comparative surface temperature analysis was performed by

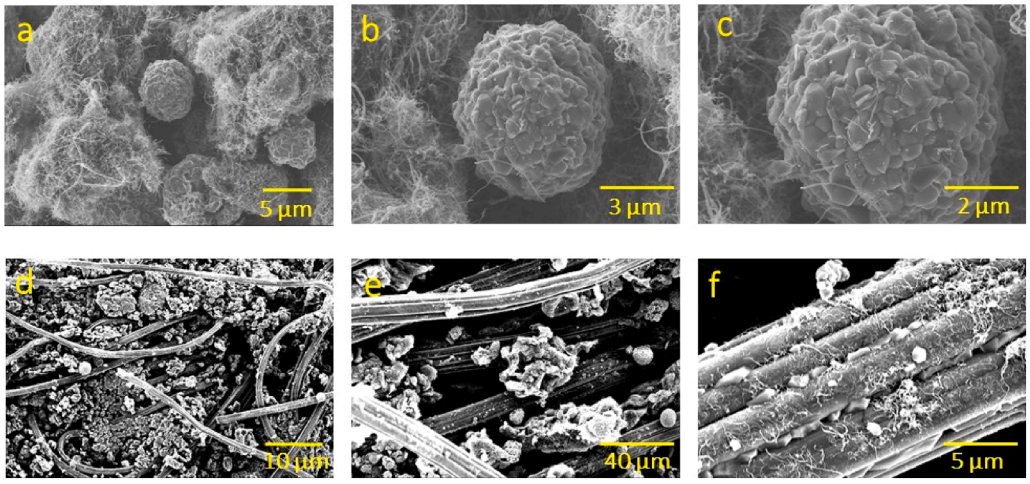

Fig. 3. SEM images of the NCAL@CNT composite powder. (a-c) Morphology of the NCAL@CNT composite powder at different magnifications. (d-f) Morphology of the NCAL@CNT-Non-woven fabric at different magnifications.

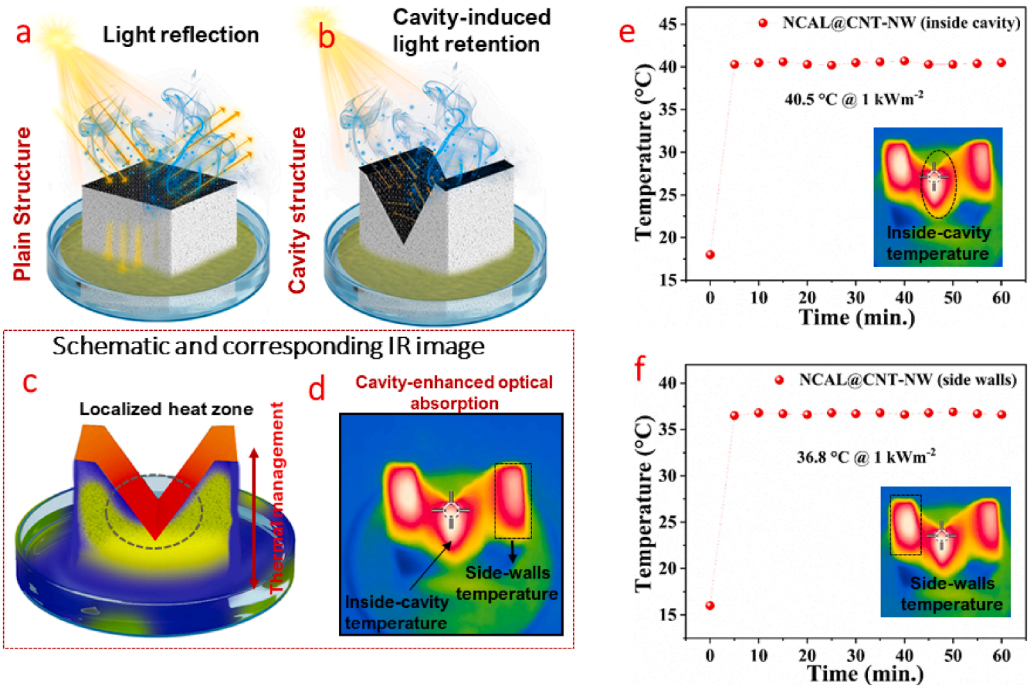

Fig. 4. Optical and thermal management advantages of the V-shaped cavity design. (a) Schematic of a flat evaporator showing significant light reflection. (b) Schematic of the V-shaped cavity evaporator, where incident light is trapped *via* multiple internal reflections. (c) Schematic illustration of the localized heat zone within the cavity. (d) Corresponding infrared thermal image confirming heat concentration at the base of the V-shaped cavity. (e) Time-dependent temperature profile at the base (inside) of the cavity under 1 sun illumination. (f) Time-dependent temperature profile on the sidewall of the V-shaped cavity under 1 sun illumination.

recording surface temperatures on the side walls and inside the cavity of the NCAL@CNT-NW evaporator under 1 sun intensity. Upon irradiation, the temperature at the cavity's base (Fig. 4e) rose quickly from an ambient ~16 °C to 40.5 °C, and achieved equilibrium state. Similarly, the temperature on the cavity walls (Fig. 4f) stabilized at about 36.8°C. The inside-cavity region reaches a higher steady-state temperature (~40.5 °C) compared to the side walls (~36.8 °C), demonstrating effective heat localization within the cavity structure. This behavior arises from the integrated cavity geometry, which promotes light trapping and multiple internal reflections, leading to enhanced energy absorption and reduced heat dissipation. The infrared images further confirm that thermal energy is concentrated in the cavity region rather

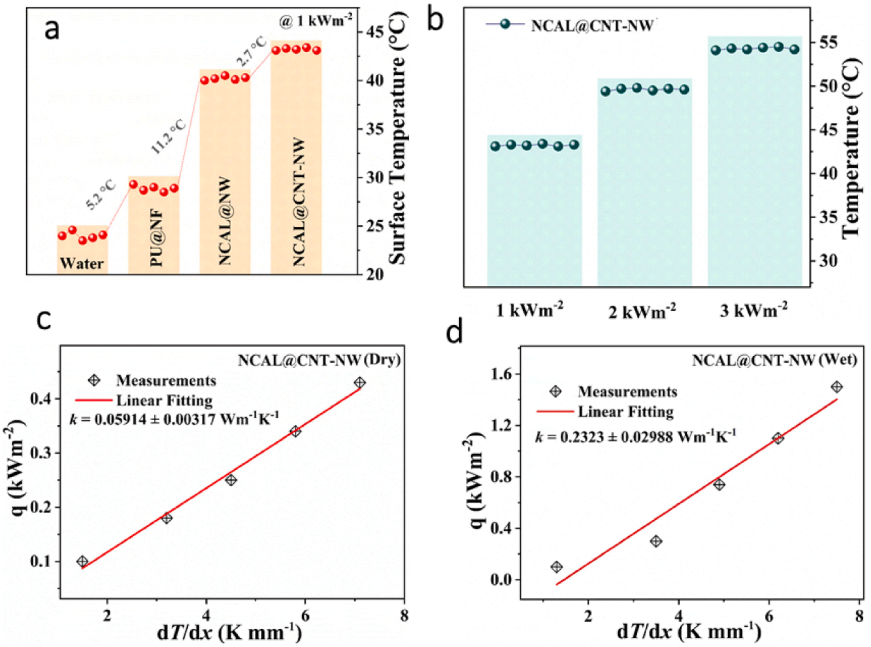

Fig. 5. Quantitative thermal performance of the evaporator system. (a) Steady-state surface temperature of different system configurations under 1 sun illumination, highlighting the incremental contribution of each component. (b) Surface temperature of the NCAL@CNT-NW evaporator under varying solar intensities (1, 2, and 3 sun), demonstrating scalable photothermal response. (c) Thermal conductivity measurement of the dry NCAL@CNT-NW fabric. (d) Thermal conductivity measurement of the water-saturated (wet) NCAL@CNT-NW fabric.

than spreading outward. Such geometry-assisted heat confinement is beneficial for improving evaporation efficiency by maximizing localized heating and minimizing thermal losses [16].

In addition, a thorough quantitative examination of the NCAL@CNT evaporator's thermal performance is presented in Fig. 5, which establishes a direct correlation between the material and structural design of the device and its capacity for energy conversion. The data validates the system's responsiveness under varied solar flux and methodically demonstrates each component's synergistic contribution to the overall photothermal impact, two crucial metrics for assessing realistic solar-driven applications. Each functional layer's contribution is evident in the incremental surface temperature rise under 1 sun irradiation (Fig. 5a). The addition of the insulating PU foam and non-woven fabric (PU@NW) increased the temperature by 5.2 °C in comparison to the bulk water surface (~22 °C). This demonstrates the essential function of thermal insulation in lowering conductive and convective losses. The intrinsic photothermal activity of the nickel-rich oxide is highlighted by the coating of NCAL alone (NCAL@NW), which caused an additional notable spike of 11.2 °C, reaching ~40 °C. An additional 2.7 °C rise to around 43 °C was obtained by integrating CNTs with NCAL (NCAL@CNT-NW). The final enhancement demonstrates the synergistic role of CNTs to improve light absorption across the spectrum and thermal conductivity within the composite layer, which results in more effective heat generation and distribution at the evaporation interface. Fig. 5b confirms that the evaporator's performance is scalable with solar intensity. The steady-state surface temperature increased from around 43 °C at 1 sun to about 50 °C at 2 sun and then to about 54.5 °C at 3 sun illuminations, demonstrating a distinct and continuous positive connection with irradiance. The robustness and reproducibility of the photothermal response are confirmed by the minimal variance across six repeated observations at each intensity.

The system's ability to efficiently harness larger energy input is demonstrated by this linear trend, which is a crucial prerequisite for practical application under natural, variable sunshine. During both dry and wet conditions, the evaporator's thermal transport characteristics were accurately characterized (Fig. 5c-d). In the dry state, the NCAL@CNT composite layer exhibited a very low thermal conductivity of $k_{dry} = 0.05914 \pm 0.00317$ W $m^{-1}K^{-1}$. This characteristic is highly advantageous as it limits lateral heat dissipation from the illuminated spot, promoting vertical heat concentration towards the water interface. When saturated with water (wet state), the thermal conductivity increased substantially to $k_{wet} = 0.2323 \pm 0.02988$ W $m^{-1}K^{-1}$.

Moreover, an important visual and quantitative evaluation of the thermal dynamics and geographical heat distribution during the solar

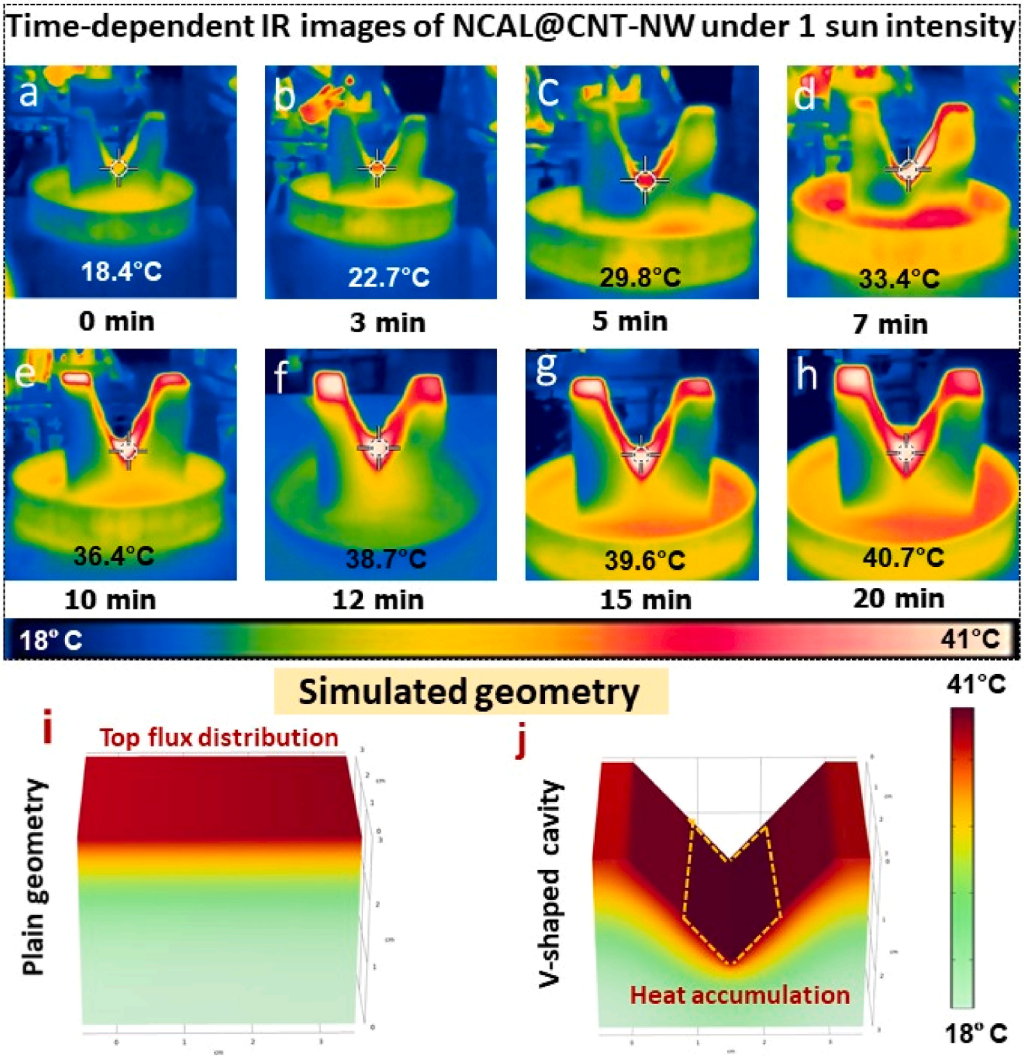

Fig. 6. Time-dependent infrared thermal images of the NCAL@CNT-NW evaporator under 1 sun illumination. (a) 0 min, (b) 3 min, (c) 5 min, (d) 7 min, (e) 10 min, (f) 12 min, (g) 15 min, (h) 20 min. The image series verifies consistent heat distribution throughout the active evaporation surface and shows the quick photothermal reaction, reaching a stable surface temperature of about 40.7 °C. (i) The COMSOL simulation of the steady-state temperature distribution for a (i) plain (flat) geometry, (j) V-shaped cavity.

evaporation process is provided by the time-resolved infrared (IR) thermographic analysis shown in Fig. 6. In order to eliminate unwanted lateral heat dissipation that would reduce system efficiency and to validate effective heat localization, the idea of restricting converted thermal energy to the evaporation interface, this real-time mapping is crucial. The fast photothermal reaction and the NCAL@CNT-NW evaporator's transition to a stable thermal state under 1 sun's light are clearly depicted in the series of infrared photos (Fig. 6a–h). The material's effective and quick conversion of solar energy into heat was demonstrated by the surface temperature rising significantly from an ambient 18.4 °C at t = 0 min to 29.8 °C within the first 5 min (Fig. 6a–c). High photothermal conversion efficiency and efficient thermal insulation from the underlying PU foam are indicated by this quick initial temperature rise. Subsequently, the rate of temperature increases moderately as the system approaches thermal equilibrium (Fig. 6d-h). At 7 min, the temperature was 33.4 °C; at 12 min, it was 38.7 °C; by 20 min, it had stabilized at about 40.7 °C. The system reached a steady state where the combined energy losses from vaporization, radiation, and convection balanced the incoming solar energy, as seen by the transition from rapid heating to a stable plateau. The temperature distribution of the evaporator's exposed surface inside the V-shaped cavity is consistently uniform in the infrared photographs. This spatial uniformity demonstrates how well the cavity design and NCAL-CNT composite covering distribute heat uniformly, avoiding isolated "hot spots" or "cold spots" that can cause ineffective or uneven evaporation. These photos clearly confirm the successful use of the interfacial heating approach, which is essential to obtaining a high and steady evaporation rate, by showing the continuous, high temperature limited to the evaporator surface.

To further elucidate the role of structural design on heat transfer, we performed COMSOL Multiphysics heat transfer simulations for both plain and V-shaped cavity-based NCAL@CNT-NW evaporators. The geometry was constructed to represent the experimental foam dimensions, with the top surface coated by an NCAL@CNT- photothermal layer. In the final structure, a V-shaped cavity was introduced to mimic the fabricated design, while the plain structure retained a flat interface. The simulations were carried out under a uniform solar heat flux of 1 kW m^{-2}, with the ambient temperature fixed at 18 °C and convective heat transfer applied at the air interface. Material properties such as thermal conductivity, density, and specific heat of PU foam and NCAL@CNT coating were used based on reported literature values. The detailed thermal distribution calculations are given in Supporting Note S1. The goal of the simulation was to compare the thermal field distribution between the two architectures under identical illumination conditions.

As shown in Fig. 6**i**, the plain structure results in pronounced heat accumulation on the top surface, with the majority of absorbed solar energy localized at the air–solid interface. This concentrated heat leads to inefficient utilization of the absorbed energy, as the temperature gradient is not well distributed within the evaporator. Consequently, such a design favors localized heating but restricts uniform thermal transport, which may limit vapor generation efficiency and long-term operational stability. In contrast, the V-shaped cavity structure (Fig. 6**j**) demonstrates a fundamentally different heat transfer behavior, revealing that heat is preferentially accumulated inside the cavity, facilitating the flux redistribution around the cavity walls. This geometry promotes light trapping, enhances localized photothermal conversion, and ensures more uniform heat confinement within the active region. By effectively coupling optical absorption and thermal management, the V-shaped cavity structure minimizes heat loss and maximizes the driving force for water evaporation. These results validate the experimental IR observations and confirm that the V-shaped cavity architecture offers a distinct advantage over flat designs by integrating both light-harvesting and heat-localization mechanisms.

The water evaporation rate and photothermal conversion efficiency, the solar evaporator's final performance criteria, are quantified in Fig. 7. By converting the measured thermal properties into useful water production capabilities, our results directly demonstrate the functional superiority attained by the synergistic combination of the NCAL-CNT photothermal layer and the V-shaped cavity. The cumulative mass loss

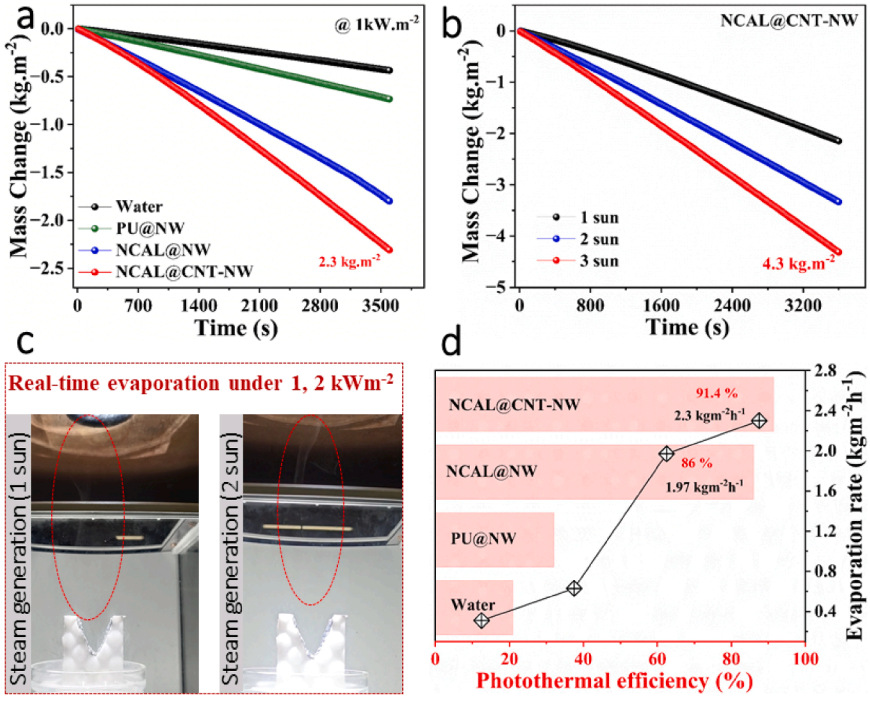

Fig. 7. Evaporation performance and energy efficiency. (a) Cumulative mass loss of different system configurations under 1 sun illumination over 1 h. (b) Cumulative mass loss of the NCAL@CNT-NW evaporator under varying solar intensities (1, 2, and 3 suns). (c) Photographs showing real-time vapor generation from the NCAL@CNT-NW evaporator under 1 and 2 suns. (d) Calculated evaporation rates and corresponding photothermal conversion efficiencies for the key material configurations.

under 1 kW m^{-2} irradiation (Fig. 7a) clearly shows how each additional functional component improves performance. The insulating PU@NW structure enhanced water yield and decreased heat loss as compared to pure water. The NCAL coating (NCAL@NW) produced a notable jump, confirming its potent photothermal action. Over the course of an hour, the NCAL@CNT-NW configuration produced the greatest cumulative mass change of 2.3 kg m^{-2}, demonstrating the crucial role that CNTs play in improving light absorption and heat distribution inside the composite. There is a clear cause-and-effect link between better thermal management and increased evaporation production because this pattern is exactly in line with the gradual temperature increases shown in Fig. 5a. A crucial feature for practical use is the evaporation rate's scalability with solar flux. The mass loss for the NCAL@CNT-NW evaporator rose significantly with irradiation, as seen in Fig. 7b, reaching approximately 3.12 kg m^{-2} at 2 sun illumination and approximately 4.3 kg m^{-2} at 3 sun illumination. This near-linear scalability, which is corroborated by photographic proof of intense steam generation at higher intensities (Fig. 7c), shows how resilient the system is and how well it can use larger solar energy inputs. Fig. 7d summarizes the steady-state evaporation rates and associated energy conversion efficiencies. With an efficiency of 86%, the NCAL@NW fabric had a remarkable evaporation rate of 1.97 kg m^{-2} h^{-1}. The NCAL@CNT-NW fabric's performance was further enhanced by the incorporation of CNTs, reaching a remarkable efficiency of 91.4% and a rate of 2.3 kg m^{-2} h^{-1}. The standard error propagation analysis was calculated and given in Supporting Note S2. With little environmental loss, this high efficiency means that more than 91% of the incoming solar energy is used for the phase transition of water.

The NCAL@CNT-NW evaporator's crucial anti-salt-fouling capacity, which is a crucial factor in determining long-term operational stability in practical desalination, is shown in Fig. 8. A significant problem for traditional interfacial solar evaporators is resolved by the capacity to reject crystallized salt and avoid photothermal surface blockage, ensuring sustained evaporation performance. 1.3 g of NaCl crystals were directly loaded onto the NCAL@CNT-NW fabric's surface under 1 sun illumination to conduct a thorough salt rejection test. The self-cleaning behavior is visually confirmed by the time-series photographic record (Fig. 8a-h). White salt crystals initially filled the surface (t = 0 min). A pristine photothermal layer with no salt buildup was left behind after these crystals steadily decreased over time and were entirely dissolved and removed from the surface in 300 min. This demonstrates the evaporator's effective salt rejection in high-salinity conditions. The underlying mechanism enabling this performance is illustrated in Fig. 8i-j. The design promotes ions (Na^+, Cl^-) to continuously diffuse downward away from the evaporation front. This is caused by a combination of factors: the capillary flow of water through the porous PU foam and fabric constantly provides fresh water to the interface, while the intense localized heating at the surface causes a strong evaporation-driven convection. A concentration gradient is created by this convection, where the salinity at the hot evaporation surface rises above that of the bulk water below. As a result, dissolved ions spontaneously migrate along this concentration gradient, returning to the bulk solution from the high-salinity zone at the interface. This dynamic mechanism ensures unobstructed light absorption, water supply, and vapor escape for long-lasting operation by preventing the supersaturation and precipitation of salts on the evaporator surface. Two complementary stability tests were carried out to assess the possibility of long-term recurrent use. The evaporator was operated for 15 days under one sun. The stability and salt resistance of the CNT-NW system were extensively assessed in saline environments. As illustrated in Fig. 8k, the evaporation rate was recorded over multiple days under various saline conditions. Despite exposure to salty water, the evaporation rate remained consistent at around 1.6–2.0 kg m^{-2} h^{-1} over the testing period. This steady performance in saline circumstances implies good salt rejection and continued ion transport inside the porous structure. The findings indicate that the NCAL@CNT-NW evaporator can maintain high evaporation efficiency while resisting salt-induced deterioration, indicating its applicability for practical desalination applications. Furthermore, 30 consecutive cycles of a cyclic test were conducted as shown in Fig. 8l. At cycle 1, the initial rate of evaporation was 2.25 kg m^{-2} h^{-1}. The rate was as high as

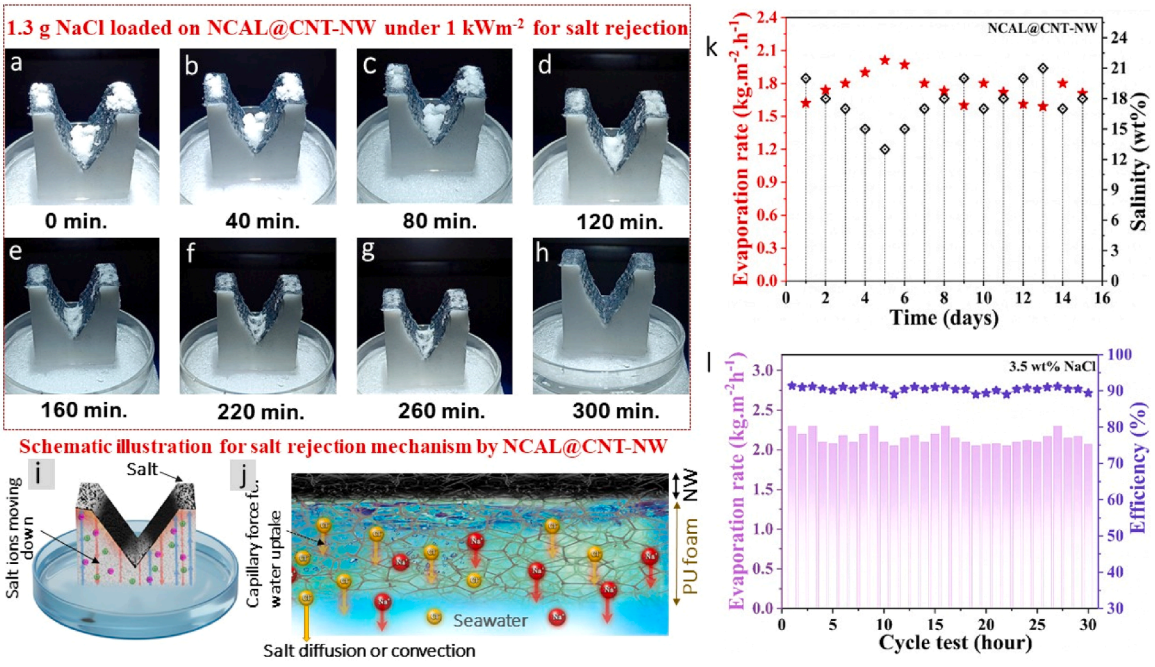

Fig. 8. Salt rejection performance and mechanism. (a-h) Time-series photographs showing the dissolution and clearance of 1.3 g of pre-loaded NaCl crystals from the NCAL@CNT-NW fabric surface under 1 sun illumination over 300 min. (i) Schematic of the complete evaporator setup illustrating the downward diffusion of Na^+ and Cl^- ions. (j) Detailed mechanism schematic showing capillary water supply to the evaporation interface and the concurrent back-diffusion of ions into the bulk water, preventing salt accumulation. (k) Long-term evaporation rate and bulk water salinity of the NCAL@CNT-NW evaporator. (l) Cyclic performance of the NCAL@CNT-NW evaporator over 30 cycles in 3.5 wt% NaCl solution.

2.02 kg m^{-2} h^{-1} after 30 cycles, maintaining around 90% of the original performance. With relatively slight fluctuations throughout the course of the 30 cycles, the corresponding photothermal conversion efficiency remained close to 90%. The strong mechanical integrity of the PVA-binder-assisted NCAL@CNT coating and the self-cleaning feature of the V-shaped cavity, which stops salt-induced photothermal layer deterioration, are responsible for this exceptional cyclic stability.

The NCAL@CNT-NW evaporator's multifunctional performance and practical viability outside of controlled laboratory settings are validated in Fig. 9. It illustrates the system's remarkable ability to generate high-purity freshwater from complex feedwater, its adaptability in handling a variety of complex water sources, and its strong performance under actual, changing environmental conditions. Photographs of active steam generation are used to initially demonstrate the evaporator's outdoor capability (Fig. 9a-b). This performance is measured via a thorough 10-hour diurnal test (8:00–18:00) in natural sunshine (Fig. 9c). The recorded evaporation rate tracked solar intensity, peaking at approximately 1.05 kg m^{-2} h^{-1} at midday (~570 W m^{-2}) and tapering off as the sun set. Importantly, despite simultaneous changes in wind speed (3.5–9.2 m h^{-1}) and ambient humidity (41.5–57.5%), the system continued to operate steadily, demonstrating its resistance to real-world climatic conditions that usually reduce efficiency. Furthermore, the lower solar irradiation experienced outside (peak ~570 W m^{-2} versus 1000 W m^{-2} in the lab) is the main cause of the lower peak evaporation rate seen outside (1.05 kg m^{-2} h^{-1}) compared to the lab value (2.30 kg m^{-2} h^{-1}). The predicted rate of 1.31 kg m^{-2} h^{-1}, which is marginally greater than the observed 1.05 kg m^{-2} h^{-1}, is obtained by scaling the lab performance by the irradiance ratio. The discrepancy can be explained by additional environmental heat losses that are not present in the controlled lab setting, specifically wind (up to 9.2 m h^{-1}) and lower ambient temperature. Simple steps like a transparent wind screen around the evaporator and better side insulation could be used to reduce these losses in real-world applications, bringing outside performance closer to the theoretical prediction. These improvements are simple and will be investigated in subsequent research to optimize practical efficiency. Fig. 9d and e provide a thorough quantification of the purifying capabilities, which is a key benefit of this multifunctional design. Common ion concentrations were drastically reduced in the condensate from simulated high-salinity water: Na^+, K^+, Mg^{2+}, and Ca^{2+} were lowered from thousands of mg L^{-1} to less than 2 mg L^{-1}, exceeding

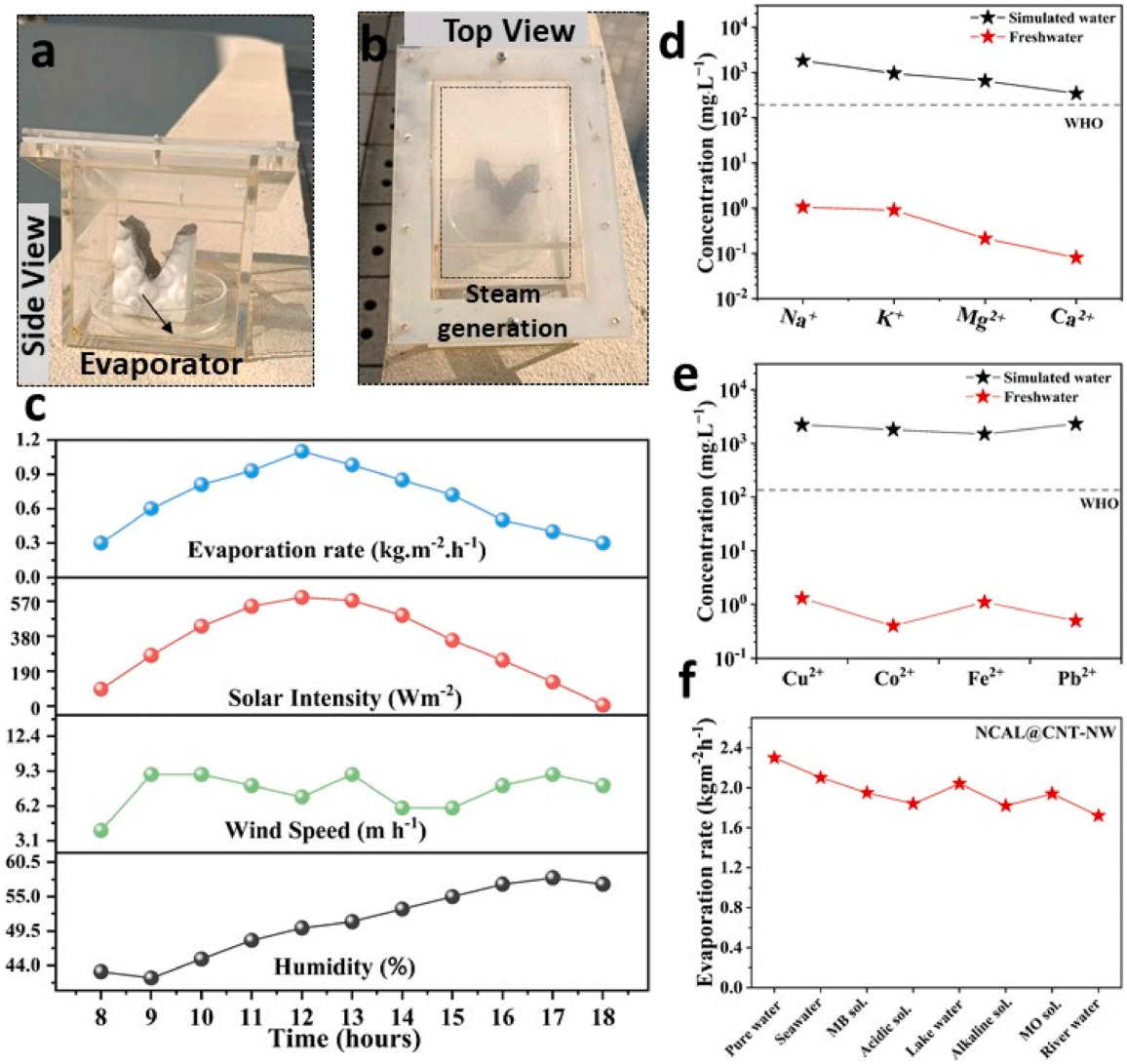

Fig. 9. Outdoor practical performance and comprehensive water purification assessment. (a-b) Photographs of the evaporator during outdoor testing show side and top views of steam generation. (c) Diurnal variation of key environmental parameters (solar intensity, humidity, wind speed) and the corresponding evaporation rate over a 10-hour outdoor test. (d) Concentration of common ions (Na^+, K^+, Mg^{2+}, and Ca^{2+}) in simulated seawater feed and the collected freshwater condensate. (e) Concentration of heavy metal ions (Cu^{2+}, Co^{2+}, Fe^{2+}, and Pb^{2+}) in simulated wastewater feed and the collected freshwater condensate. (f) Evaporation rate of the NCAL@CNT-NW evaporator measured in various water sources, demonstrating its versatility.

99.9% rejection and satisfying WHO drinking water requirements. More importantly, the evaporator showed remarkable effectiveness in eliminating hazardous heavy metal ions. Cu^{2+}, Co^{2+}, Fe^{2+}, and Pb^{2+} concentrations were likewise lowered to almost or less than 1 mg L^{-1}, indicating rejection efficiencies greater than 99.97%. Lastly, a variety of practical and challenging water sources were used to assess the evaporator's adaptability (Fig. 9f). In freshwater (2.3 kg m^{-2} h^{-1}) and seawater simulation (2.1 kg m^{-2} h^{-1}), it maintained significant evaporation rates. With rates ranging from 1.7 to 1.9 kg m^{-2} h^{-1}, it also demonstrated strong performance in contaminated media, such as dye solutions (methyl orange, methylene blue), acidic/alkaline solutions, and actual lake/river water. The solutes' little light absorption or scattering is the reason for the somewhat lower rates in chemically complex or colored waters. This steady performance highlights the system's potential as an off-grid, worldwide method of obtaining freshwater from almost any source, combining rigorous purification with high output. Moreover, the evaporation rate closely followed the solar intensity with no symptoms of performance decline, indicating stable functioning under realistic variable conditions, despite the outside test being carried out during a single daytime cycle (10 h). This stability is consistent with the accelerated salt-rejection test (Fig. 8), which verified efficient self-cleaning, and the materials' strong performance in acidic and alkaline environments (Fig. 9f), which demonstrated chemical resistance. Future research will confirm the long-term chemical and physical endurance of the photothermal coating and PU foam through extended multi-day cycling tests, including nighttime recovery.

3.1. Stability and metal leaching assessment

For practical applications, the NCAL-CNT evaporator's long-term stability is crucial, especially due to the possibility of transition metal (Ni, Co) leaching in chemically harsh environments [29,30]. As seen in Fig. 9**f,** the evaporation performance was assessed in both acidic (pH 3) and alkaline (pH 11) environments. In both media, the evaporator maintained steady evaporation rates of 1.8 kg m^{-2} h^{-1}, which are only marginally less than the rate in neutral freshwater (2.3 kg m^{-2} h^{-1}). This consistent performance shows that even in chemically demanding conditions, the composite structure is still functional and intact. Previous research on $LiNi_{0.8}Co_{0.15}Al_{0.05}O_2$ (NCA) supports the stability of the NCAL component in aquatic settings. When exposed to water, NCA particles naturally create a protective Li_2CO_3 surface layer that prevents nickel and cobalt from dissolving further [31]. Additionally, the NCAL particles are encapsulated by the polyvinyl alcohol (PVA) binder employed in the production, which lessens direct water interaction and further reduces the possibility of metal leaching [32]. The metal concentrations in the condensate throughout the evaporation tests were determined by ICP-OES to be below the detection limit (0.01 mg L^{-1} for both Ni and Co), which is well within the WHO drinking water recommendations (Ni: 0.07 mg L^{-1}; Co: 0.05 mg L^{-1}) [33]. These findings verify that secondary metal contamination is not introduced during operation by the NCAL-CNT evaporator.

3.2. Economic feasibility considerations

The multifunctional performance shown in this work justifies the usage of battery-grade NCAL (purity > 99.8%), even if it is more expensive than traditional carbon-based photothermal materials [34–36]. The NCAL-CNT composite concurrently achieves a high evaporation rate (2.30 kg m^{-2} h^{-1}, 91.4% efficiency), > 99.9% removal of heavy metal ions (Pb^{2+}, Cu^{2+}, Co^{2+}, Fe^{3+}), and excellent salt self-cleaning, in contrast to carbon-only evaporators that mainly address salinity. This eliminates the need for separate water treatment units, thereby offsetting the initial material cost. Additionally, the actual material cost per device remains low because the active material loading per evaporator is very low (~100 mg of NCAL, based on a 1:1 mass ratio with CNTs, for a 200 mg total composite). A long operational lifetime improves the lifecycle cost-benefit ratio because of the strong structural integrity and steady performance over prolonged operation (Fig. 9c) [37,38]. Economies of scale are anticipated to significantly lower unit costs as NCA materials are mass-produced for the electric car market [39]. In order to improve economic feasibility without compromising performance, future research could investigate the use of recycled or lower-purity NCAL from wasted lithium-ion batteries.

4. Conclusion

In conclusion, we have successfully developed a novel V-shaped NCAL@CNT-NW photothermal heat harvesting fabric by incorporating NCAL decorated with multi-walled CNTs onto a hydrophilic nonwoven fabric. The synergistic combination of the composite's excellent photothermal properties and the V-shaped cavity's heat-trapping capability resulted in a system that effectively localizes thermal energy at the water-air interface. This design achieved an exceptional evaporation rate of 2.30 kg m^{-2} h^{-1} with a corresponding solar-thermal conversion efficiency of 91.4% under 1 sun illumination. Furthermore, the evaporator demonstrated robust anti-salt-fouling performance, where preloaded salt crystals were completely dissolved and rejected within 300 min, ensuring long-term operational stability. While the current study shows excellent salt-rejection and stable operation during a full daytime cycle, future work will involve multi-day cyclic tests under alternating day-night circumstances to further validate long-term durability for practical deployment. Beyond pure water production, the system exhibited outstanding multifunctional purification capabilities, effectively removing over 99.9% of common seawater ions (Na^+, K^+, Mg^{2+}, and Ca^{2+}) and toxic heavy metal ions (Cu^{2+}, Co^{2+}, Fe^{2+}, and Pb^{2+}). The evaporator also maintained stable performance across diverse water sources, including seawater, acidic/alkaline solutions, and dye-contaminated water, and under real, fluctuating outdoor conditions. This work presents a significant advancement in solar-driven water purification technology, moving beyond simple desalination to address complex water contamination.

CRediT authorship contribution statement

Huibin Guan: Conceptualization, Writing – original draft. **Naila Arshad:** Formal analysis, Writing – review & editing. **Bushra Shakoor:** Formal analysis, Writing – review & editing. **Najah Alwadie:** Formal analysis. **Xiaochao Fan:** Conceptualization, Funding acquisition, Project administration, Resources, Supervision, Writing – original draft. **Ruijing Shi:** Investigation. **Van-Duong Dao:** Project administration, Supervision. **Nang Xuan Ho:** Validation. **Jian Zhang:** Project administration. **Muhammad Sultan Irshad:** Investigation, Resources, Writing – review & editing. **Calvyn T. Howells:** Validation. **Phuong Anh Lam:** Visualization. **Iftikhar Ahmed:** Conceptualization, Funding acquisition, Project administration, Supervision, Writing – original draft.

Declaration of Competing Interest

The authors declare that they have no known competing financial interests or personal relationships that could have appeared to influence the work reported in this paper.

Acknowledgements

This work was financially supported by the Department of Science and Technology of Hubei Province, China (No. 2024BAB096), Princess Nourah bint Abdulrahman University Researchers Supporting Project number (PNURSP2026R478), Princess Nourah bint Abdulrahman University, Riyadh, Saudi Arabia. This work was financially supported by the National Natural Science Foundation of China: Research on Integrated Energy System of Hydrogen Storage Coupled with Coal Chemical Industry in Xinjiang (52266018); Xinjiang Engineering University's

Doctoral Start-up Fund Project: Research on Regional Integrated Energy Systems with Hydrogen Storage (2023XGYBQJ01). This work was financially supported by the Vietnam National Foundation for Science and Technology Development (NAFOSTED) (grant number 103.02–2021.106) and PHENIKAA Innovation Foundation (PU2025. PIF.03).

Appendix A. Supporting information

Supplementary data associated with this article can be found in the online version at doi:10.1016/j.jece.2026.122865.

Data availability

Data will be made available on request.

References

[1] W.W.A.P. (United Nations), UN-Water, Water for a Sustainable World: The United Nations World Water Development Report 2015, UNESCO, 2015.
[2] H. Ghasemi, G. Ni, A.M. Marconnet, J. Loomis, S. Yerci, N. Miljkovic, G. Chen, Solar steam generation by heat localization, Nat. Commun. 5 (2014) 4449, https://doi.org/10.1038/ncomms5449.
[3] M. Elimelech, W.A. Phillip, The future of seawater desalination: energy, technology, and the environment, Science (80) 333 (2011) 712–717.
[4] L. Cui, P. Wang, H. Che, J. Chen, B. Liu, Y. Ao, Solar-driven interfacial water evaporation for wastewater purification: Recent advances and challenges, Chem. Eng. J. 477 (2023) 147158.
[5] M.A. Ali, M.S. Irshad, G. Maqsood, N. Arshad, N. Aslam, M.S. Asghar, B. Shakoor, I. Hussain, M.H. Younes, T. Mei, V.D. Dao, X. Wang, Advances in flat-band structures for enhanced photothermal conversion efficiency: design, mechanism, and complementary applications, Nano Energy 142 (2025) 111297.
[6] J.M. Gohil, K. Dutta, Photothermal materials and membranes for solar-driven water treatment, Elsevier (2025).
[7] T. Umeyama, H. Imahori, Carbon nanotube-modified electrodes for solar energy conversion, Energy Environ. Sci. 1 (2008) 120–133.
[8] B. Shakoor, M.S. Irshad, U. Ghazanfar, H. Razzaq, N. Arshad, G. Maqsood, I. Ahmed, M.A. Ali, M.S. Asghar, I. Ahmed, Recent advances in conducting polymers for hybrid solar-driven evaporation systems: fundamentals, innovations, and applications, Chem. Eng. J. (2025) 169273.
[9] Y. Duan, M. Weng, W. Zhang, Y. Qian, Z. Luo, L. Chen, Multi-functional carbon nanotube paper for solar water evaporation combined with electricity generation and storage, Energy Convers. Manag. 241 (2021) 114306.
[10] M.S. Irshad, X. Wang, M.S. Abbasi, N. Arshad, Z. Chen, Z. Guo, L. Yu, J. Qian, J. You, T. Mei, Semiconductive, flexible MnO2NWs/chitosan hydrogels for efficient solar steam generation, ACS Sustain. Chem. Eng. 9 (2021) 3887–3900, https://doi.org/10.1021/acssuschemeng.0c08981.
[11] M. Das, D. Das, S. Sil, P.P. Ray, Development of hierarchical copper sulfide–carbon nanotube (CuS–CNT) composites and utilization of their superior carrier mobility in efficient charge transport towards photodegradation of Rhodamine B under visible light, Nanoscale Adv. 5 (2023) 3655–3663.
[12] S. Lal, S.K. Batabyal, Activated carbon-cement composite coated polyurethane foam as a cost-efficient solar steam generator, J. Clean. Prod. 379 (2022) 134302.
[13] S.U. Muzayanha, C.S. Yudha, A. Nur, H. Widiyandari, H. Haerudin, H. Nilasary, F. Fathoni, A. Purwanto, A fast metals recovery method for the synthesis of lithium nickel cobalt aluminum oxide material from cathode waste, Metals 9 (2019) 615.
[14] N. Arshad, M.S. Irshad, M. Alomar, J. Tao, X. Wang, G. Zhenzhen, M.A.K. Shah, M. S. Asghar, U. Ghazanfar, H.X. Nang, Z. Ouyang, N. Mushtaq, V.-D. Dao, J. Guo, H. Wang, A Sustainable Solar Evaporation Strategy: Higher Condensate Yields Through Remote Condensing Structure via Polyelectrolyte Solar Evaporator, Adv. Funct. Mater. n/a (n.d.) 2509989. https://doi.org/https://doi.org/10.1002/adfm.202509989.
[15] X. Wang, Q. Gan, R. Chen, H. Peng, T. Zhang, M. Ye, Water delivery channel design in solar evaporator for efficient and durable water evaporation with salt rejection, ACS Sustain. Chem. Eng. 8 (2020) 7753–7761.
[16] J. Lin, M. Wu, H. Fang, M. Wu, S. Li, H. Zhang, Y. Jiang, F. Huang, Scalable, bio-inspired and self-floating bi-layer polyurethane foam solar evaporator with excellent capillary hydrodynamic effect, Chem. Eng. J. 482 (2024) 148909.
[17] S. Liu, S. Li, Q. Yang, M. Lin, Scale-up of solar interfacial evaporation devices: advanced optical, thermal, and water management for efficient seawater desalination, Energy Environ. Sci. 18 (2025) 9446–9456.
[18] M.S. Asghar, M.S. Irshad, N. Arshad, M. Al Huwayz, M. Alomar, G. Maqsood, M. A. Ali, U. Ghanzanfar, M. Sabir, J. Li, V.D. Dao, N.X. Ho, X. Wang, Z. Guo, Functionalized carbon nanotubes interconnected with metal-organic frameworks for in-situ solar-driven evaporation and salt recovery from seawater, Water Res 282 (2025) 123643.
[19] M.S. Irshad, X. Wang, N. Arshad, M.Q. Javed, T. Shamim, Z. Guo, H.R. Li, J. Wang, T. Mei, Bifunctional in situ polymerized nanocomposites for convective solar desalination and enhanced photo-thermoelectric power generation, Environ. Sci. Nano 9 (2022) 1685.
[20] V. Biju, M. Abdul Khadar, Electronic structure of nanostructured nickel oxide using Ni 2p XPS analysis, J. Nanopart. Res. 4 (2002) 247–253.
[21] N. Eswaramoorthy, P.K. Muthusamy, A. Kareem, A.P. Shyma, S. Nallusamy, P. Sathishkumar, V. Elangovan, Resurfaced nickel alloy: a stable and efficient catalytic electrode for oxygen evolution reaction, Mater. Lett. 406 (2025) 139855.
[22] T. Jiang, I.A. Poimenidis, D. Luo, C. Jiang, Q. Zhao, R. Bakker, W. Li, M.C.A. Stuart, P. Arendsen, X. Zhang, M. Konsolakis, V. Kyriakou, Synergistic effects of Ni^{3+}–Cu0/+ dual sites for efficient and stable hydrogen production in AEM water electrolysis, Appl. Catal. B Environ. 389 (2026), https://doi.org/10.1016/j.apcatb.2026.126597.
[23] B. Zhang, R. Hu, D. Sun, T. Wu, Y. Li, Fabrication of chitosan/magnetite-graphene oxide composites as a novel bioadsorbent for adsorption and detoxification of Cr (VI) from aqueous solution, Sci. Rep. 8 (2018) 15397, https://doi.org/10.1038/s41598-018-33925-7.
[24] G. Chen, W. Sun, Y. Luo, H. Liu, S. Geng, K. Yu, G. Liu, Investigation of layered $Ni_{0.8}Co_{0.15}Al_{0.05}LiO_2$ in electrode for low-temperature solid oxide fuel cells, Int. J. Hydrog. Energy 43 (2018) 417–425.
[25] R.S. Prasannakumar, V.I. Chukwuike, K. Bhakyaraj, S. Mohan, R.C. Barik, Electrochemical and hydrodynamic flow characterization of corrosion protection persistence of nickel/multiwalled carbon nanotubes composite coating, Appl. Surf. Sci. 507 (2020) 145073.
[26] Y.-K. Sun, S.-T. Myung, B.-C. Park, J. Prakash, I. Belharouak, K. Amine, High-energy cathode material for long-life and safe lithium batteries, Nat. Mater. 8 (2009) 320–324.
[27] L. Wang, Z. Peng, J. Li, Y. Chen, J. Dong, Z. Chi, D. Li, C. Yang, Study on the performance of spent LiNi1/3Co1/3Mn1/3O2 repaired via in situ conversion and coating of surface lithium impurities, Electrochim. Acta (2025) 146990.
[28] G. Liu, Q. Wu, X. Liu, X. Zhan, G. Fu, C. Tang, Z. Liu, High-performance electro-optic manipulation by plasmonic light absorber with nano-cavity field confinement, IEEE Photonics J. 13 (2021) 1–9.
[29] W.B. Hawley, A. Parejiya, Y. Bai, H.M. Meyer III, D.L. Wood III, J. Li, Lithium and transition metal dissolution due to aqueous processing in lithium-ion battery cathode active materials, J. Power Sources 466 (2020) 228315.
[30] N.V. Faenza, Z.W. Lebens-Higgins, P. Mukherjee, S. Sallis, N. Pereira, F. Badway, A. Halajko, G. Ceder, F. Cosandey, L.F.J. Piper, Electrolyte-induced surface transformation and transition-metal dissolution of fully delithiated LiNi0. 8Co0. 15Al0. 05O2, Langmuir 33 (2017) 9333–9353.
[31] K. Kimura, K. Onishi, T. Sakamoto, K. Asami, M. Yanagida, Achievement of the high-capacity retention rate for the Li [Ni0. 8Co0. 15Al0. 05] O2 (NCA) cathode containing an aqueous binder with CO2 gas treatment using the cavitation effect (CTCE), J. Electrochem. Soc. 166 (2019) A5313–A5317.
[32] T. Watanabe, T. Yokokawa, M. Yamada, S. Kurosumi, S. Ugawa, H. Lee, Y. Irii, F. Maki, T. Gunji, J. Wu, F. Matsumoto, Surface coating of a LiNixCoyAl1−x−yO2 (x> 0.85) cathode with Li3PO4for applying a water-based hybrid polymer binder during Li-ion battery preparation, RSC Adv. 11 (2021) 37150–37161.
[33] W.H. Organization, Guidelines for drinking-water quality: first addendum to the fourth edition, (2017).
[34] I. Redhwi, S. Almalki, H. Radhwi, Advancements in battery technology: a comprehensive review, Clean. Energy Sci. Technol. 4 (1) (2026) 573. Energy 4 (2026) 573.
[35] M.N. AlMallahi, M.Y.E. Selim, M. Elgendi, Interfacial solar evaporation using biomass: environmental impact, financial feasibility, and a bibliometric perspective, Desalination 614 (2025) 119160.
[36] H.U. Modekwe, O. Olaitan Ayeleru, M.A. Onu, N.T. Tobias, M.A. Mamo, K. Moothi, M.O. Daramolad, P.A. Olubambi, The current market for carbon nanotube materials and products. Handb. Carbon Nanotub, Springer, 2021, pp. 1–15.
[37] M. Werner, M. Markanovic, C.-S. Ciesla, L. Brandb, Economic analysis of market opportunities for CNTs and nanodiamond, Carbon-Based Nanomater. Hybrids Synth. Prop. Commer. Appl. 2014 (2014) 171.
[38] Y. Li, G. Lan, Activated carbon and carbon black. Carbon Catal, CRC Press, 2024, pp. 47–110.
[39] O. Winjobi, J.C. Kelly, Q. Dai, Life-cycle analysis, by global region, of automotive lithium-ion nickel manganese cobalt batteries of varying nickel content, Sustain. Mater. Technol. 32 (2022) e00415.